Direct determination of paraquat herbicide by square-wave voltammetry by two-step transfer mechanism at heterogeneous boron-doped carbon nanowall electrodes

Sourav Sain [a], Mateusz Ficek [b], Adrian Olejnik [b,c], Mirosław Sawczak [c], Robert Bogdanowicz [b,*], Susanta Sinha Roy [a,*]

[a] Department of Physics, School of Natural Sciences, Shiv Nadar Institution of Eminence (SN IoE), Deemed to be University, Delhi-NCR, Greater Noida 201314, India
[b] Department of Metrology and Optoelectronics, Faculty of Electronics, Telecommunications and Informatics, Gdansk University of Technology, 11/12 G. Narutowicza Street, 80-233 Gdansk, Poland
[c] Szewalski Institute of Fluid-Flow Machinery, Polish Academy of Sciences, Fiszera 14, Gdansk, Poland

ABSTRACT

Boron-doped carbon nanowalls (B:CNW) versus boron-doped diamond (BDD) materials were investigated for the effective electrochemical detection of highly toxic herbicide paraquat (PQ). Depending on the surface morphology and functional groups of BDD and B:CNWs, the electrochemical absorption and detection of the target analyte PQ revealed different detection mechanisms. The surface absorption mechanism was mainly observed for BDD, while for B:CNWs, both surficial and edge absorption were observed due to the sharp edges of carbon nanowalls. This effectually drives the high heterogenous electron transfer kinetics at absorption sites. Detection of PQ was carried out in phosphate buffer solution with an optimized pH of 10 and parameters of the square-wave voltammetry. Comparative studies show higher voltammetric current peak heights for B:CNWs (~90.5 μA) than BDD (~7.5 μA) at a much lower PQ concentration of 4 μM. B:CNWs show a higher sensitivity of 11 μA/μM/cm^2 than BDD of 2.23 μA/μM/cm^2, hence BDD shows a LOD of 1.8 μM, whereas B:CNWs have a much lower LOD of 0.47 μM. Density functional theory calculations (DFT) show a higher propensity of the B:CNW models toward electrocatalytic reduction of the PQ. Moreover, the proposed two-step detection mechanism is strongly supported by the distribution of the PQ electrostatic potential in different oxidation states in conjunction with the slab surfaces. The higher the sensitivity, the lower the LOD, and the excellent performance of B:CNWs in the detection of PQ in real water samples also suggests its potential for use in the environmental monitoring and assessment of emerging pollutants.

1. Introduction

Pesticides and herbicide residues are increasing at an alarming rate, leading to hazards for human health and other life forms [1]. Meeting the increase in food growth due to the increase in population has led to extensive use of these pesticides and herbicides. Among other herbicides, paraquat (PQ) is one of the most acutely toxic pesticides widely used in more than 130 countries [2–4]. Paraquat has very high mortality rate due to ineffectiveness in treatment by any drug. Excess exposure may damage brain, heart, lungs, liver, and kidney [5]. Herbicides such as paraquat require attention due to their non-biodegradability and resistance to microbial degradation in nature, which adds up to their toxicity. Paraquat causes lung, kidney, and organ failure in humans, and so is limited to only 10 μg/L in water bodies [6,7].

Previously, many spectroscopic-based detectors were designed for the detection of such herbicides as paraquat. Pyridine-based fluorescent sensors were developed based on the intermolecular interaction of paraquat. Calorimetric-based sensors were also designed for the detection of paraquat using synthesized Imida-AgNPs with an LOD of 6.27 μM. Other spectroscopic methods, such as liquid chromatography [8] and gas chromatography mass spectroscopy, were also used for the detection of paraquat. Paraquat was detected using UV–Vis spectroscopy assisted by $Fe_3O_4@SiO_2$ nanoparticles [9]. Most of the spectroscopic methods include prior chemical treatment and lab-based equipment.

These methods are time-consuming, required trained, skilled manpower, involve lengthy detection processes, and are much costlier, limiting point-of-care testing (POCT) applications. Electrochemical-based sensors serve the POCT-based analysis as they are usually portable, have high sensitivity, and have short analysis times. Among the other electrochemical-based methods, square-wave voltammetry (SWV) is the strongest potential method with rapid and sensitive diagnosis, and environmental and food analysis in various fields of biosensing [10–12]. There are various studies into the electrochemical-based sensing of PQ using carbon-based electrodes. These carbon-based electrodes are further doped with nitrogen or boron to enhance the performance of the working electrode. One example is Fe_2O_3, which was decorated on boron/nitrogen doped on carbon nanosheets to enhance the electrochemical sensing of PQ in natural water [11]. Pillararene coated nitrogen-doped carbon nanodots showed enhanced performance for the detection of PQ [12]. The development of new carbon-based materials is crucial to further enhance the electrochemical sensing performance with higher sensitivity and selectivity. This work mainly focuses on carbon-based material doped with nitrogen or boron, which includes boron-doped diamond (BDD) and boron-doped nanowalls (B:CNWs). The comparative study will confirm the performance of these respective electrodes, paving the way for more advanced carbon-based materials.

BDD and B:CNWs are two of the promising carbon-based materials for biosensing. Various other carbon-based materials mostly obtained through chemical treatment are susceptible to fouling. Other reported work has used nanodiamonds on polymer surfaces to enhance the antifouling in biosensing, which confirms the antifouling nature of diamond-based electrodes. BDD and BCNW have shown enhanced antifouling effects in electrochemical biosensing along with high stability, a low background current and a wide potential window [13–15]. The biodetection of organophosphate pesticides was performed using acetylcholinesterase-based gold nanoparticle-modified BDD [16]. BDD-based electrodes were also incorporated into a microfluidic platform for lab-on-a-chip sensing of environmental contaminants [17]. B:CNWs are one of the most promising materials grown similarly to BDD using multi step plasma growth techniques by MW PE CVD systems. Earlier studies have shown B:CNWs have enhanced electrochemical properties as well as enhanced sensitivity for the electrochemical biodetection of paracetamol [18]. B:CNWs have also shown higher electron transfer kinetics and current than glassy carbon electrodes and undoped carbon nanowalls for electrochemical sensing of guanine and adenine [19]. The performance of B:CNWs for the detection of organophosphate pesticide, such as PQ, is yet to be studied. Until now, there is no reported work based on the electrochemical sensing of PQ by B:CNW-based carbon electrodes. This study will introduce another potential carbon-based electrode for the management of biohazards in the environment.

In this work, a comparative study was performed using B:CNW and BDD surfaces for the electrochemical detection of PQ. This comparative study was performed to investigate the enhanced-performance electrode materials among boron-doped diamond-based electrodes for the sensitivity- and selectivity-enhanced electrochemical sensing of PQ. The comparison of surface morphology and surface functionalization of BDD and B:CNWs were conducted using FE-SEM, Raman Spectroscopy, and XPS to confirm the differences in surface morphology and functional groups. The Raman spectroscopy of both materials provides insights into the carbon footprints. The peak currents were improved through the optimization of experimental parameters, such as the pH and deposition potential. Various concentration ranges for the detection of PQ were performed to confirm the linear range of operation along with LOD. Finally, real sample analysis was tested in spiked water samples using the best-performing electrode materials within the linear range chosen from lower concentration ranges. The underlying mechanistic causes of the enhancement are investigated using density functional theory (DFT) calculations of electronic structure and electrostatic potential maps for the PQ molecule and slab models of real BDD and B:CNW electrodes.

2. Experimental details

2.1. Materials and reagents

All chemicals and reagents used for experimental purposes were of LR grade and above. Potassium Ferrocyanide ($K_4[Fe(CN)_6].3H_2O$), Potassium ferricyanide ($K_3[Fe(CN)_6]$), and Potassium phosphate monobasic (KH_2PO_4) were bought from CHEMLABS. Di-Potassium hydrogen ortho-phosphate (K_2HPO_4) was brought from FINAR. Potassium hydroxide was bought from Sigma-India. Paraquat Pentasal (PQ) was of high ACS grade and was bought from Sigma-Aldrich.

2.2. Apparatus

The surface morphology analysis for both BDD and B:CNWs were studied using FE-SEM (JEOL, USA). The electrochemical performances were studied with a three electrode setup where the counter electrode was platinum, the reference electrode was Ag/AgCl, and the working electrode was the BDD or B:CNWs. The instrumental setup used for the electrochemical studies was a 302 N potentiostat/galvanostat (Metrohm Autolab B.*V*., Utrecht, the Netherlands). XPS measurements were carried out using a Thermo Fisher scientific system (Al-kα source, hν = 1486.6 eV). Raman measurements were performed using a Raman microscope (InVia, Renishaw, UK). Spectra were recorded over the range 200–3500 cm^{-1} with an integration time of 5 s (10 averages) using an argon ion laser emitting at 514 nm and operating at 10 % of its total power (50 mW).

2.3. Fabrication procedure for BDD and B:CNWs.

BDD and B:CNW were synthesized using an MWPECVD system (SEKI Technotron AX5400S, Japan). Both BDD and B:CNW thin films were grown on (100)-oriented silicon substrates. During the process, the substrate holder was heated up to 700 °C by an induction heater, which was controlled by a thermocouple. The fabrication process was carried out at a pressure of 50 Pa and microwave power up to 1300 W. The detailed parameters of the thin film synthesis can be found elsewhere, for the BDD in [20,21] and the B:CNW in [22,23].

2.4. Electrochemical analysis

The detection of PQ was carried out in a three-electrode electrochemical setup with a 6.5 mL solution using the SWV method at room temperature. Both the samples BDD and B:CNWs were used as pristine without any further surface treatments. A stock solution of PQ of concentration 1 mM was prepared in water. The stock solution was further diluted in phosphate buffer solution (PBS, 0.1 M) to lower the concentration. The pH optimization was carried out with a pH range of 6 to 11 at a PQ concentration of 50 μM. The deposition potential was optimized at a PQ concentration of 50 μM, corresponding to the selected optimized pH value. The reduction mainly occurs due to the presence of two quaternary nitrogen atoms in the PQ dication (PQ^{2+}). The first reduction from PQ^{2+} occurs when it accepts one electron to become PQ^+ and then accepts one more electron to form the neutral PQ^0 compound. The PQ^+ present can also react with dissolved oxygen to form PQ^{2+} ($2PQ^+ + 1/2O_2 + H_2O \rightleftharpoons 2PQ^{2+} + OH^-$). There are primarily two cathodic peaks, corresponding to $PQ^{2+} + e^- \rightleftharpoons PQ^+$ (PQ_1) and $PQ^+ + e^- \rightleftharpoons PQ^0$ (PQ_2) [24]. The liner detection limit was investigated experimentally by the concentration of PQ in PBS (0.1 M). The detailed three electrode system with the working electrodes, BDD and B:CNWs are shown in Scheme 1. The practical use of B:CNWs was investigated by real sample analysis. The water sample was directly collected from tap (SNIoE, India). The pH was set corresponding to the electrochemically optimized value. This water was further spiked with different concentrations of PQ and investigated along with the presence of all other impurities naturally available.
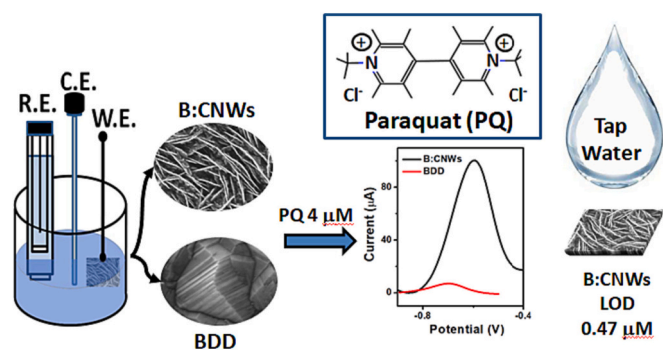
Scheme 1. Detection of PQ in water samples by using BDD and B:CNWs.

2.5. DFT model design

Molecular structures of PQ molecules and slabs were built in the Atomistic ToolKit Quantumwise (ATK, Synopsys, USA) environment. Density functional theory (DFT) computations were performed using the Perdew–Burke–Ernzerhof (PBE) functional within the generalized gradient approximation (GGA), as implemented in the package. The Linear Combination of Atomic Orbitals (LCAO) method [25] with double-zeta polarized ATK basis set and FHI norm-conserving pseudo-potentials were applied [26]. Density of states spectra for isolated PQ molecules were calculated using multipole boundary conditions (single k-point). Electron density maps and electrostatic potential maps were plotted using the default tool implemented in the ATK package.

Adsorption simulations were conducted via geometry optimizations of the PQ molecule placed above the slab with 0.05 eV/Ang force tolerance, where the four topmost layers were allowed to relax and all deeper layers fixed. This methodology was described in detail in our recent work [27]. Such adsorption calculations were performed for three types of surfaces – diamond (220), flat graphite (0002), and vertically oriented graphite (11−20). Diamond (220) slabs consisted of 201 carbon atoms within a $10.1 \times 17.8 \times 6.3$ Ang^3 box. Flat graphite (0002) slabs consisted of 217 carbon atoms within a $14.8 \times 14.8 \times 10.1$ Ang^3 box. Vertical graphite (11−20) consisted of 193 carbon atoms within a $17.1 \times 13.4 \times 7.$ Ang^3 box. For all the slabs, a 25 Ang vacuum was placed above the surface to avoid interactions of the periodic images. Both pristine and boron-doped slabs were used to investigate the different influences of boron doping on the adsorption energy. Two boron atoms per slab (1 % total concentration) were placed either at the surface layer or inside the 3rd or 4th layer, depending on the simulation.

Adsorption energies were calculated according to the standard formula (1):

$$E_{ads} = E_{slab-PQ} - E_{slab} - E_{PQ} \qquad (1)$$

In general, diamond (220) slabs are models of the BDD electrode and the mixture of all three slabs can be seen as the model of the real BCNW.

3. Results and discussion

3.1. Surface morphology and composition of BDD and B:CNWs

The surface morphology of the grown B:CNWs and BDD samples deposited by MW-PECVD was analyzed by FE-SEM. Fig. 1(a) and (b) shows the surface morphology of B:CNWs and BDD with differences in surface morphology. Polycrystalline BDD films exhibit a complex topography that is characterized by a heterogeneous and textured surface composed of many diamond crystallites or grains with varying orientations and morphologies. The individual grains show numerous shapes and sizes, ranging from 200 nm to 1 μm in diameter, and are densely packed or sparsely distributed. The crystals reveal faceted surfaces with sharp edges leading to the formation of a more homogeneous

surface [28,29].

The walls formed in the B:CNW films exhibit an unusual morphology characterized by nearly straight structures, which is distinct from the maze-like CNW formations reported by other studies. The incorporation of boron in the films had a significant influence on the length and number of walls, as shown in Fig. 1(a). The average wall length was estimated to be around 1 μm. The increased quantity of walls resulted in a denser film with higher specific capacitance due to the presence of small pores between the nanowalls [30]. B:CNWs are complex 3D structures with multilayered graphene oriented vertically on the substrate surface. The individual agglomerates of carbon clusters were observed to cover the sides of the flat carbon walls. Additionally, the growth mechanism of these carbon clusters was explained by the formation of nanocrystalline or ultra-nanocrystalline diamond structures [31]. This structural feature is likely responsible for the enhanced charge transfer, which can deliver improved sensing capabilities. Earlier reported work has also shown that BDD is a sp^2-rich material, whereas B:CNWs are a sp^3 material [28,29].

The surface characteristics of BDD and BCNW were carried out using high-resolution XPS spectroscopy for comparison of the surface properties, as both differ in their chemical composition. Fig. 1(c) shows the XPS spectroscopy analysis for B:CNWs and BDD. The XPS images of B:CNWs in Fig. 1(c) show the presence of C=C at 284.4 eV, C—C at 285.1 eV, C—O/C—N at 283.6 eV, and a small peak for C—B at 283.3 eV for the B:CNW samples [19]. C=C at 284.4 eV, C—C at 285.0 eV, and C—O at 286.5 eV were also observed for the BDD samples. The presence of C—N and C—B bonds in the B:CNWs shows more doping of nitrogen and boron than for the BDD. It was observed that there is a greater presence of sp^2 carbon bonds (45.38 %) than sp^3 carbon (35.39 %) in the B:CNWs. Whereas there is a greater presence of sp^3 carbon (52.7 %) than sp^2 carbon (44.9 %) for the BDD samples, as shown in Fig. 1(c). The sp^2/sp^3 ratio for the BCNW and BDD were found to be 1.28 and 0.85, which signifies the presence of more defect states for the B:CNW-based electrodes [32]. The presence of more defect states enhances the absorption rate of the target analyte PQ onto the surface of the B:CNWs.

Raman spectra reveal the main differences in the crystalline structure of the BDD and BCNW. Fig. 1(d) shows the Raman spectroscopy of the BDD and B:CNWs samples with details of the peaks in Table 1. For the boron-doped diamond, the broad and intense band centered near 500 cm^{-1} (B1) dominates in the low wavenumber range. This band is related to boron dimers and clusters of boron atoms located in the diamond lattice [33,34]. The boron-carbon complexes also manifest themselves through the band located near 1200 cm^{-1} (B2) that overlaps with a band related to the presence of defects in the diamond structure [35]. The zone center optical phonon band of diamond (B3) with its maximum near 1320 cm^{-1} is redshifted in the case of the BDD in relation to the diamond line (1332 cm^{-1}) due to the Fano effect. The band (B4) located near 1536 cm^{-1} can be assigned as a G band that is related to the sp^2 carbon phase [36]. The D carbon band that is expected near 1350 cm^{-1} cannot be resolved in the Raman spectra of the BDD.

In the case of the B:CNWs, the Raman pattern significantly differs from the spectra of the BDD and is dominated by two intense bands centered near 1350 and 1580 cm^{-1} that are related, respectively, to the D band corresponding to the breathing mode of sp^2 atoms in a ring, and the G band associated with bond stretching of sp^2 atoms in rings and chains. For the visible Raman excitation (514 nm in our case), both the D and G bands are primarily related to the sp^2 phase. The intensity of the D band correlates with the amount of disorder of sp^2-hybridized atoms in graphite-like materials. For graphite-like structures, the boron doping did not induce significant changes in the crystalline structure, and only a slight decrease in the interlayer spacing of the graphite (002) was reported [37]. In the Raman spectra, boron doping is manifested mainly in an increase of the D band and is related to defect-induced modes [38]. These properties of B:CNWs can be correlated with the XPS spectroscopy, as discussed previously.
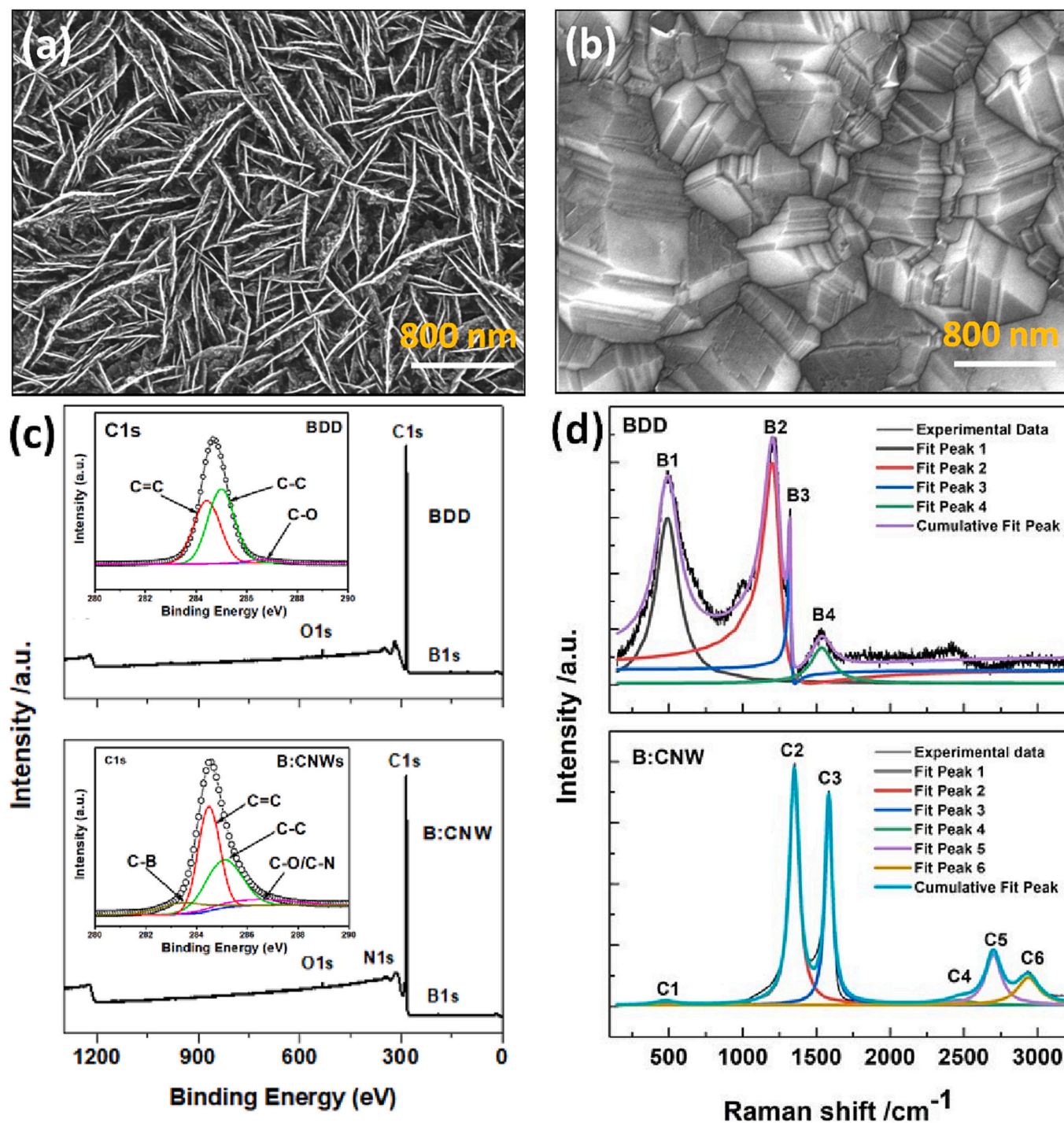
Fig. 1. Surface morphology comparison by FE-SEM images of (a) B:CNWs and (b) BDD. Composition and structural analyses conducted by (c) X-ray photoelectron spectroscopy and XPS peaks fitting for B:CNWs and BDD. (d) Raman spectroscopy and Raman peaks deconvolution for B:CNWs and BDD.

3.2. Electrochemical characterization of BDD and B:CNWs

The B:CNW and BDD samples were investigated using cyclic voltammetry (CV) to evaluate the electron transfer kinetics and electrochemical active surface area. The aqueous PBS solution of pH 10 was probed with ferro/ferri redox agent at a concentration of 5 mM. The C*V* analysis for the B:CNWs was performed with a potential range of -0.2 V to 0.6 V from a scan range of 10 mV/s to 100 mV/s, as shown in Fig. 2(a). Similarly, CV scans for the BDD were performed within a potential range of -0.3 V to 0.7 V from a scan rate of 10 mV/s to 100 mV/s, as shown in Fig. 2(c). Fig. 2(a) and (c) shows the typical quasi-reversible profile of

$[Fe(CN)_6]^{3-/4-}$ with oxidation (I_{pa}) and reduction (I_{pc}) peaks [39]. For both B:CNWs and BDD, the ratio of $I_{pa}/I_{pc} \sim 1$ corresponds to the scan rate range 10 mV/s to 100 mV/s, which is a typical feature of a quasi-reversible profile. Fig. 2(b) and (d) show the liner response with the scan rate for both the B:CNWs and BDD working electrode. The linear response of the I_{pa} and I_{pc} plot with root of the scan rate is a typical characteristic of the Randel-Sevick equation, which is given by Eq. (2) [40].

$$I_{pa} = (2.69 \times 10^5) n^{3/2} A C D^{1/2} v^{1/2}$$

(2)

The electroactive surface area (A) was calculated using the slope

Table 1

Parameters of the main Raman bands are determined based on Lorentzian and Breit-Wigner-Fano (BWF) functions.

PEAK	ω	Normalized intensity	FWHM
B1	490.91	0.75	190.17
B2	1201.63	1.00	156.02
B3	1319.61	0.68	24.44
B4	1535.99	0.16	180.30
C1	477.19	0.02	155.07
C2	1350.67	1.00	79.82
C3	1583.29	0.88	59.85
C4	2476.74	0.02	204.33
C5	2700.05	0.22	130.42
C6	2937.20	0.12	181.53

which is the ratio of the peak current (I_{pa}) and the root of the scan rate (v) of the fitted curves, along with the concentration of the redox probe (C) and its diffusion coefficient (D). The values of A for B:CNWs and BDD were found to be 0.126 cm^2 and 0.66 cm^2, respectively. There was a shift in the peak potential with the increasing scan rate, which can be elucidated by the degree of interfacial redox kinetics and calculating the electron transfer coefficient (α) using the Laviron equation, as shown in Fig. S1(a) and S1(b) (supporting information). The values of (α) for B:CNWs and BDD were found to be 0.51 and 0.69, respectively, which are close to the ideal value of 0.5, which is a typical feature of a reversible redox probe exhibiting rapid heterogeneous transfer kinetics. The details of the calculations for Matsuda and Ayabe Λ and the heterogeneous electron transfer rate constant (k^0) are shown in the supporting

information. The B:CNWs show a higher k^0 value than the BDD, signifying a higher electron transfer rate, as shown in Table 2. The value for the B:CNWs lies within the range of 0.096 and 11.2, which refers to a quasi-reversible Faradaic reaction [41].

3.3. Optimization of sensor parameters to enhance performance of B: CNW and BDD samples

The sensitivity and selectivity for the electrochemical detection of PQ by BDD and B:CNWs were enhanced through experimental study of important sensor parameters. The optimization was performed at a PQ concentration of 50 µM in PBS (0.1 M) solution which was diluted from the 1 mM stock solution. Calibration of the pH and deposition potential was performed by varying them from 6 to 11 and -0.7 *V* to -1.6 V, respectively.

The detection of PQ was carried out using the SWV method, where

Table 2

Comparison of electrochemical parameters of B:CNWs and BDD at a scan rate of 100 m*V*/s^{-1}.

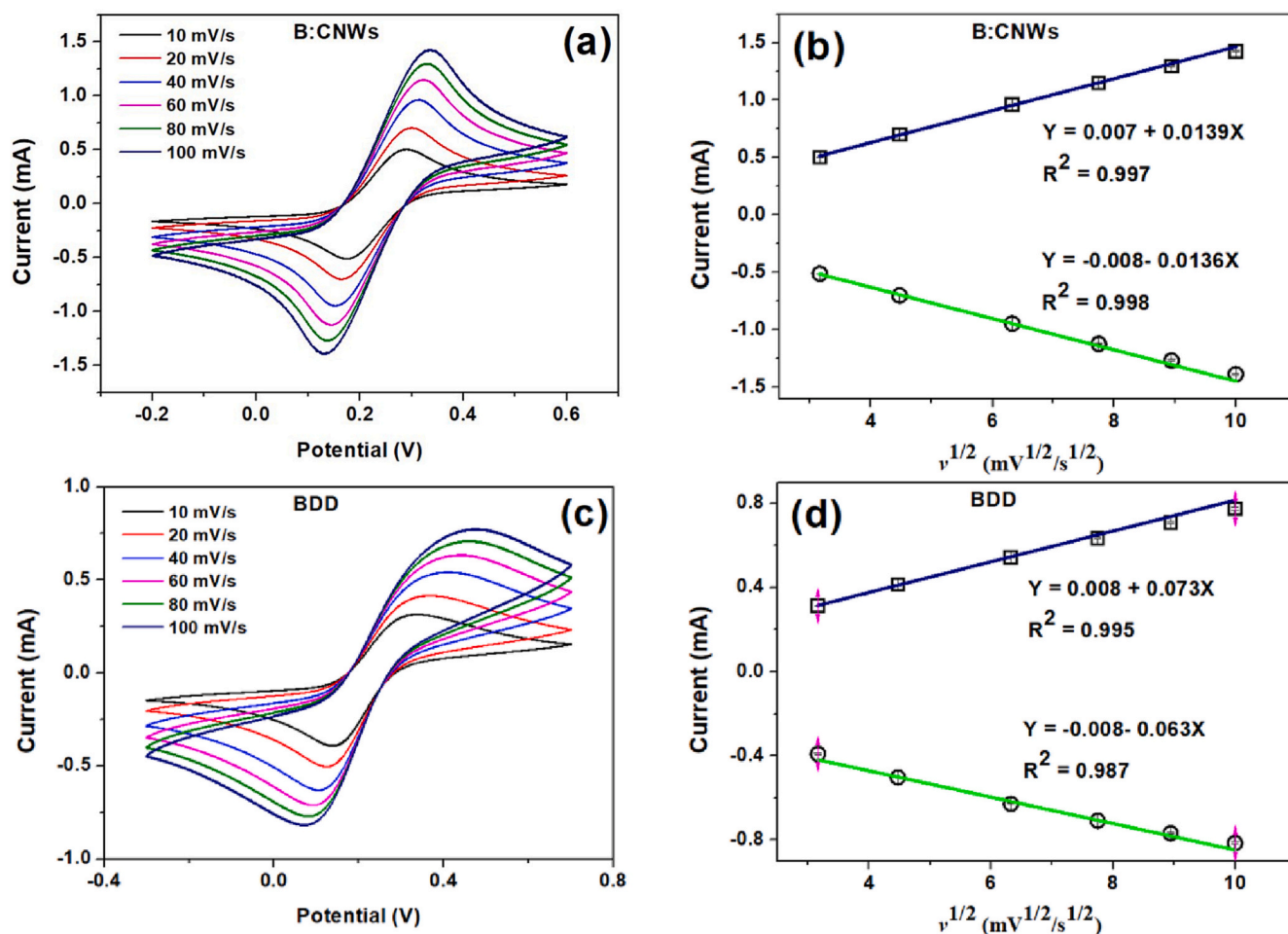|	B:CNWS	BDD
E_{pa}	0.336	0.474
E_{pc}	0.129	0.072
ΔE_p	0.207	0.402
α	0.51	0.69
k^0	9.85×10^{-4}	4.145×10^{-6}
Λ	0.194	8.16×10^{-4}

Fig. 2. Cyclic voltammetry response (a) B:CNWs, (c) BDD, effect of scan rate on peak potential (E_p) and currents (I_{pa} and I_{pc}) containing 5 mM [Fe(CN)$_6$]$^{3-/4-}$ in PBS (0.1 M) solution of pH 10 (b) B:CNWs and (d) BDD.

deposition potentials play a crucial role in enhancing the peak current. The experiments were carried out using a PQ concentration of 50 μM in PBS (0.1 M) solution. Fig. 3(a) and (b) show the optimization of deposition potential for B:CNWs and BDD with peak currents PQ$_1$ and PQ$_2$ similar to the mechanism mentioned in Section 2.4. Prominent peaks of PQ$_1$ were observed from −0.7 V for both B:CNWs and BDD. The peak current increases up to −0.9 V and −0.8 V for both B:CNWs and BDD. This increase in peak current was observed for increased accumulation PQ onto the electrode surface. Then the peak current decreases with the increase in the deposition potential. This was observed mainly due to the formation of H$^+$ ions with a pronounced negative potential, which limits the accumulation of PQ on the electrode surface. Similarly, the PQ peak corresponding to the PQ$_2$ current was observed from −1.0 V for both BDD and B:CNWs. The maximum peak current for PQ was observed to be −1.2 V for both B:CNWs and BDD. It was observed that for both B:CNWs and BDD, the PQ$_1$ is more dominant, with higher current peaks than PQ$_2$. This was probably observed due to a peak position of PQ$_2$ at a higher negative potential. This is also in line with the DFT results given in Section 3.8. as the first electron transfer is energetically more feasible on the carbon surfaces than the second. Therefore, the first electron transfer reducing PQ to PQ1 occurs in a weaker negative bias and results in a higher cathodic current.

Optimization of the pH was studied for both the BDD and B:CNWs samples corresponding to both dominant PQ$_1$ peaks. The PQ$_1$ peak currents corresponding to different pH values are shown in (Fig. 3(c) and (d) for the B:CNWs and BDD samples, respectively. The pH values were varied from 6 to 11 in a PBS (0.1 M) solution while keeping the PQ concentration fixed at 50 μM. The peak currents corresponding to PQ$_1$ increase from pH 6 to pH 10 for both BCNW and BDD working electrodes. This was mainly observed as PQ being a positive cation and at lower pH, more H$^+$ ions are present, which limits the absorption of PQ on the surface of the working electrode. A decrease in the current was observed for the B:CNW samples, which was mainly due to hydrolysis of PQ on the surface of the B:CNW samples, as shown in Fig. 3(c) [42]. A pH of 10 was selected for detecting PQ at different concentrations as B:CNWs have shown the maximum peak current at this pH and the BDD currents remained nearly constant.

3.4. Electrochemical detection of PQ by SWAV method

The detection of PQ using B:CNWs and BDD was carried out using the SWAV method in ambient temperature. The experiments were performed with different PQ concentrations in a PBS (0.1 μM) solution using only 6.5 mL of solution. The pH of the solution was fixed at 10 whereas the deposition potential was kept at −0.9 V, corresponding to PQ$_1$, as discussed in the previous section. The inset of Fig. 4(a) shows the voltammograms for B:CNW working electrodes corresponding to the reduction of PQ referred to as PQ$_1$. The peak current of PQ$_1$ was observed to increase linearly from 2 μM to 12 μM. Fig. 4(a) and (b) show the linear calibration plots for B:CNW working electrodes at different concentration ranges. It was observed that the peak current becomes nonlinear after 12 μM due to the limitation of the electrode material in the absorption of PQ on the surface. Fig. 4(c) shows similar trends for BDD working electrodes after a PQ concentration of 4 μM. The linearity plots for B:CNWs were found to be I (μA) = 8.80 C(μM) + 55.9 with a sensitivity of 11 A/M.cm^2. The lower concentration ranges for B:CNWs for PQ sensing shown in Fig. 4(b) were also performed within a linear range of 0.1 μM to 1 μM with a sensitivity of 10.28 μA/μM.cm^2 and LOD of 0.47 μM. The corresponding voltammograms are shown in inset of Fig. 4(b). The linearity plot for the BDD samples was found to be I (μA) = 1.78C (μM) + 0.59 with a LOD of 1.8 μM and sensitivity of 2.23 μA/μM.cm^2, as shown in Fig. 4(c) along with the voltammograms. The peak current of PQ for the B:CNWs was higher than for the BDD working electrodes. It can be correlated with the DFT results on the charge
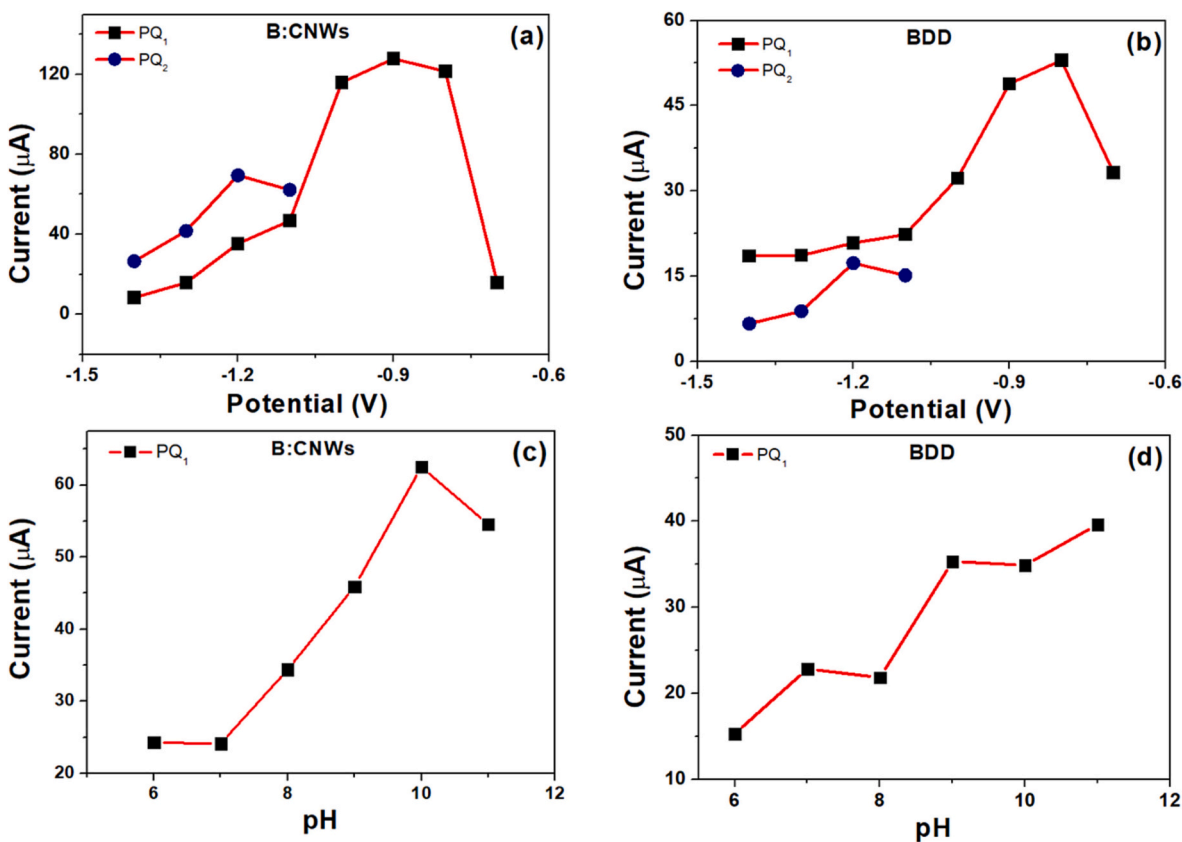

Fig. 3. Optimization of experimental parameters at a PQ concentration of 50 μM with deposition potential from −0.7 V to −1.4 V applied at the working electrode (a) B:CNWs and (b) BDD, pH varied from 6 to 11 of the PBS electrolytes at deposition potential −0.9 V for (c) B:CNWs and (d) BDD.
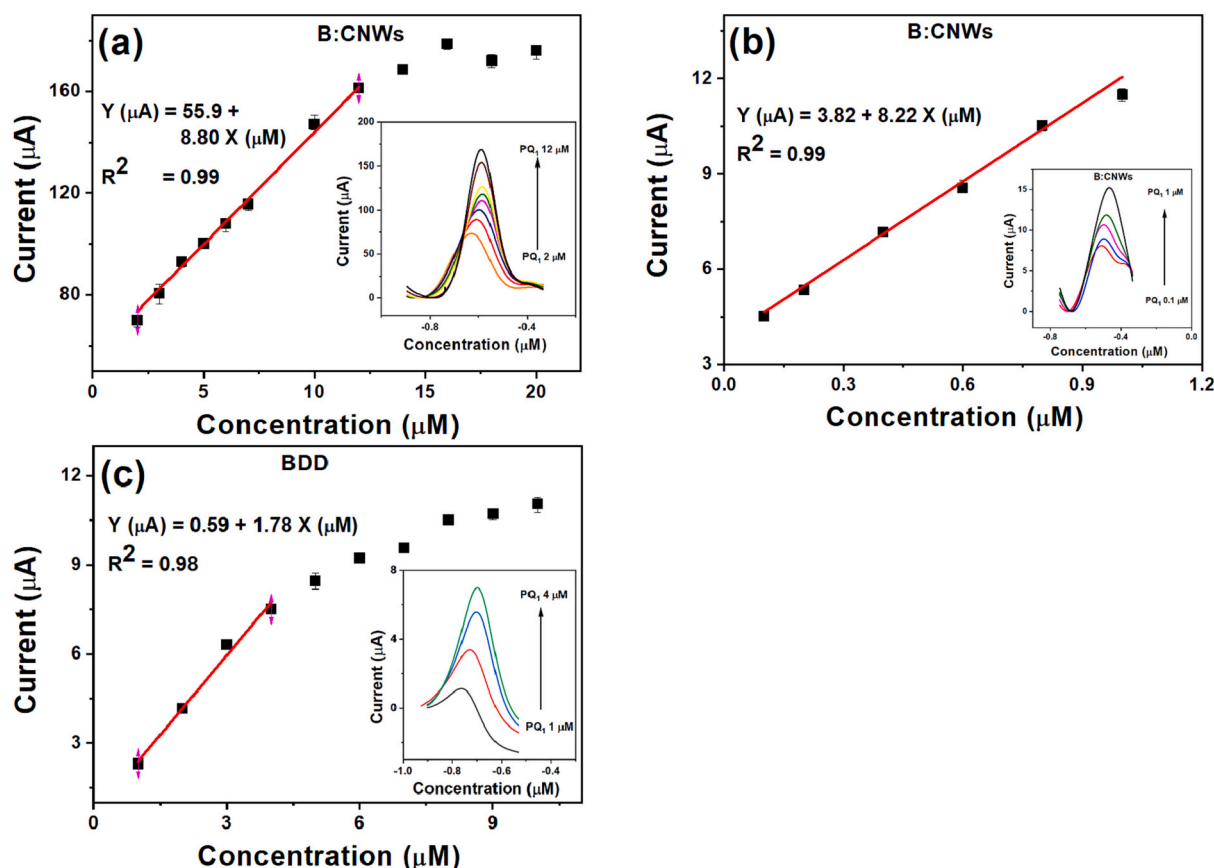
Fig. 4. SWAV response of PQ in PBS (0.1 M) solution of pH 10 for calibration plot within the linearity range for the concentration ranges (a) B:CNWs of 2–12 μM with saturation up to 12 μM, (b) B:CNWs of 0.1–1 μM, (d) BDD of 1–4 μM with saturation up to 10 μM.

transfer energies being lower for the graphitic model of the B:CNW electrode in comparison to the BDD electrode. It was observed that the peak current at a lower PQ concentration of 4 μM for B:CNWs was 90.5 μA whereas for BDD it was only 7.5 μA as shown in Fig. S2(a) (supporting information). This enhanced peak current was due to the larger surface area, as observed in the SEM images, and the presence of more graphene phase, as confirmed by the XPS analysis, for the B:CNW working electrode. Earlier reported works also confirm the enhancement of sensing properties by graphene edges due to both surface and edge adsorption of the target analyte (PQ) [43,44]. Whereas for BDD-based electrodes, there was only the surface adsorption phenomenon for the target analyte (PQ) [45]. Moreover, the DFT discussed further clearly shows that surface adsorption on the graphite edges at (11–20) planes is thermodynamically facilitated in comparison to the graphite surface at (0002) planes. Table 3 shows the comparison of different types of paraquat sensing as well as other electrochemical methods. This study shows that electrochemical-based sensors can potentially detect lower concentrations than other methods. The linearity range of the B:CNW

working electrode sits close to composite-based electrodes, as mentioned in Table 2.

3.5. Reproducibility, repeatability, and real sample analysis

The comparative study of sensing of PQ with B:CNWs and BDD showed that B:CNW samples have higher sensitivity and enhanced LOD in comparison to BDD, as discussed in Section 3.4. The stability and reproducibility study plays a crucial role in establishing B:CNW electrodes as a real-time sensing material for electrochemical-based sensors. The stability and repeatability study for the detection of PQ showed a maximum RSD of 1.4 %. The reproducibility performed at a lower concentration range of 0.4 to 0.8 μM of PQ also showed a maximum variation of 7.0 %, which lies within the range of 10 %. The practical use of B:CNWs was established with a real sample analysis in tap water samples. The procedure followed was the same as previously published research work [50]. Spiked concentration ranges of 0.4, 0.6, and 0.8 μM were used for the analysis of water samples. Table 4 shows that the maximum recovery range was within 5 % with RSD values below 5 %. The selectivity of electrochemical sensing of PQ by B:CNWs was investigated in the presence of other pesticides commonly found in water bodies. The interferent used for experimental investigation was carbofuran, thiram, bentazon and urea at an 10 times more concentration

Table 3
Comparative study for the detection of PQ with sensor parameter (linear detection range) with BDD and B:CNW-based samples.

Electrode	Method	Linear range (μM)	Reference
GR/ZnO/SPE	DPV	0.05–2	[8]
MWCNTs-DHP/GCE	SWV	0.10–1.70	[46]
PPY-NGE/GCE	DPV	0.05–2	[47]
Pyranine	FL	1–20	[48]
Sodium Montmorillonite Clay	FL	2–8	[49]
t-LIG	SWV	0.5–35	[50]
BDD	SWV	1–4	This Work
B:CNWs	SWV	0.1–1, 2–12	This Work

Table 4
Detection of PQ in real water samples.

Sample number	Added (μM)	Found (μM)	Recovery (%)	RSD (%)
1	0.4	100.5	0.402	4.64
2	0.6	95.2	0.57	0.91
3	0.8	99.7	0.79	2.05

than PQ. The variation percentage was shown in Fig. 5. Among all the pesticides urea has shown most variation of 8.99 %, with others below 5 %. The variation of interferents lies below 10 % confirming the better selectivity of B:CNWs as a working electrode for the detection of PQ.

3.6. Electronic properties of the paraquat molecule in different oxidation states

The proposed model of paraquat electrochemical sensing involves two steps: after adsorption of the PQ molecule on the electrode surface; (1) first electron transfers from the electrode to the PQ and (2) the second electron transfers from the electrode to the PQ, emulating the detection mechanism at the studied surfaces. In the following section, we will investigate the rationale for this mechanism from the density functional theory (DFT) perspective and compare the performance of this reaction to the BDD and BCNW surface models. It is to be noted that in reality, the PQ redox reaction mechanism is more complicated and strongly solvent-dependent [51]. However, its assumption is sufficient to explain the prominence of the BCNW electrodes for its detection versus BDD.

Optimized molecular structures of the PQ in different oxidation states with corresponding electrostatic potential maps are given in Fig. 6 (a) to (c). In general, the thermodynamically optimal conformation of the PQ molecule is flat with the rotational energy barrier equal to less than 100 meV. This is in line with the calculations in the works [52,53].

In the oxidized form, the PQ molecule exhibits a positive electrostatic potential distributed along the benzene ring, especially on the nitrogen atoms linked to the methyl groups and carbon atoms at the aryl-aryl connection, reaching up to +3 V. This strongly suggests that the reduction reaction – which is the basis of the sensing mechanism – would occur most likely by electron tunneling toward those particular atoms. Moreover, it explains why the detection is more efficient in neutral and negative pH values (Fig. 4) as the acidic environment is rich in positively charged and mobile hydrogen ions. Presumably, the highly positive nitrogen atoms are likely to bind the mobile protons – per analogy to the tertiary amines – hindering their ability to adsorb on the electrode surface due to steric hindrance. On the other hand, methyl groups themselves are strongly negatively charged with respect to the aromatic rings and are not likely to participate in the electrochemical process that is the basis of the detection performed in Sections 3.3 and 3.4 [54].

The density of states diagrams (Fig. 6(d) to (f)) illustrating the HOMO and LUMO levels of the isolated molecule clearly show that orbitals from nitrogen and hydrogen atoms contribute to both those levels, but the majority of the density originates from the p-type carbon orbitals. Therefore, the electrochemical charge transfer observed in the electrochemical experiments should mainly occur between carbon atoms of the surface, and carbon atoms of the molecule. Initially, at this oxidation stage, the Fermi level is located between HOMO and LUMO with an arrrox. 2 eV energy gap. When the first electron is transferred toward the PQ, the Fermi level goes up and the former LUMO orbital is now half-occupied. This outcome stays in line with the intuition that molecular orbitals should be capable of storing an even number of electrons – in this case, two.

In this partially reduced state, the distribution of the electrostatic potential across the PQ molecules changes so that inner atoms of the ring receive the relative negative charge. However, the envelope around the rings' surface is still positive, but the magnitude of the voltage is reduced to 1 V. Methyl groups also retain their negative value, but its magnitude is also reduced to −1 V. This observation suggests that the second charge transfer to the molecule should have a higher energy expense as the electrostatic drive is less intense. This is reflected in the experimental results in Section 3.4, where the second reduction is observed at −1.2 V, whereas the first one has its maximum current at −0.9 V. This intuition also coincides with the numerical values of the charge transfer energies in Table 6, which will be discussed in the next subsection.

Lastly, after the second electron transfer, the molecule is further reduced and bears a negative charge, which extends toward the perpendicular direction. On the other hand, in the direction of the methyl groups, the molecule's envelope is positively polarized with a mixed charge distribution on the methyl groups themselves. Those observations suggest that the molecule is not prone to further reduction without breaking covalent bonds as the molecule is already strongly negatively charged. This is also in line with the DOS spectra, where the Fermi level goes up even further and the shape of the newly formed LUMO orbital begins to distort and hybridize with orbitals other than 2p [53].

3.7. Modeling of PQ adsorption and reduction on BDD and BCNW electrodes

Simulations of the PQ molecule adsorption have been performed on three slabs: diamond (220), flat graphite (0002) and vertical graphite (11–20) emulating the investigated electrodes. Adsorption energies were calculated for both pristine surfaces and boron-doped ones with two different positions of boron atoms – either on the atomic surface layer or several layers beneath the surface (Table 5). The first case of doping is considered surface-boron and the latter bulk-boron doping. In connection to the experiment, the pristine boron-doped diamond (220) slab can be regarded as the model for the BDD electrode, while the mixture of boron-doped diamond and graphite constitute a model of B:CNW electrodes.

The first observation from Table 5 is that adsorption of the PQ molecule on the undoped graphite is easier than on the undoped diamond. This trend is reversed for the boron-doped carbons, as the free energy is the most negative for the diamond (220) surface regardless of the boron placement. However, plain graphite is a less favorable adsorption site than vertically oriented graphite (11–20), having free energy comparable to the diamond (220). Considering that the B:NCW electrode is composed on different planes of both graphite and diamond, one can conclude that it is not adsorption that governs the enhanced catalytic properties of the B:CNWs. In short, BDD and B:CNWs are at least similarly effective in terms of PQ adsorption.

Tendencies among thermodynamic quantities are significantly different in the case of charge transfer, though. Free energies of the first and second charge transfer of the pristine PQ molecules in a vacuum and after adsorption on the surface have been gathered in Table 6. It is easy to see that all three surfaces exhibit catalytic effects by reducing the energy required for the first charge transfer with respect to the vacuum reaction. However, graphite (0002) exhibits the largest enhancement in the free energy, being equal to 0.38 eV compared to 0.26 eV for the BDD. These results can also be correlated with the electron density maps given in Fig. 7 and indicate the superiority of the B:CNWs in terms of electron
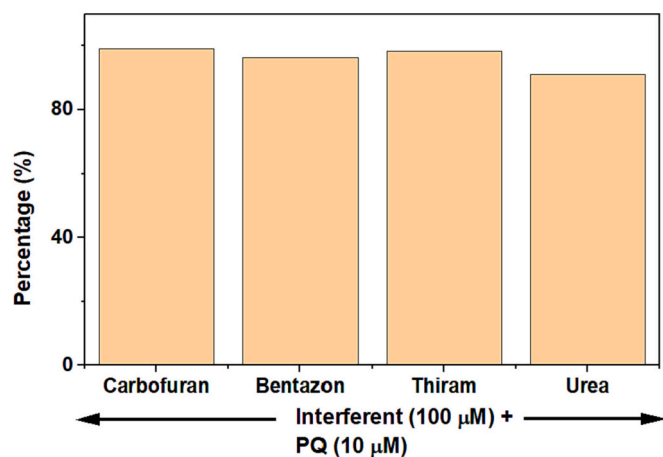

Fig. 5. Interference study with different interferents concentration of 100 μM at a PQ concentration of 10 μM.
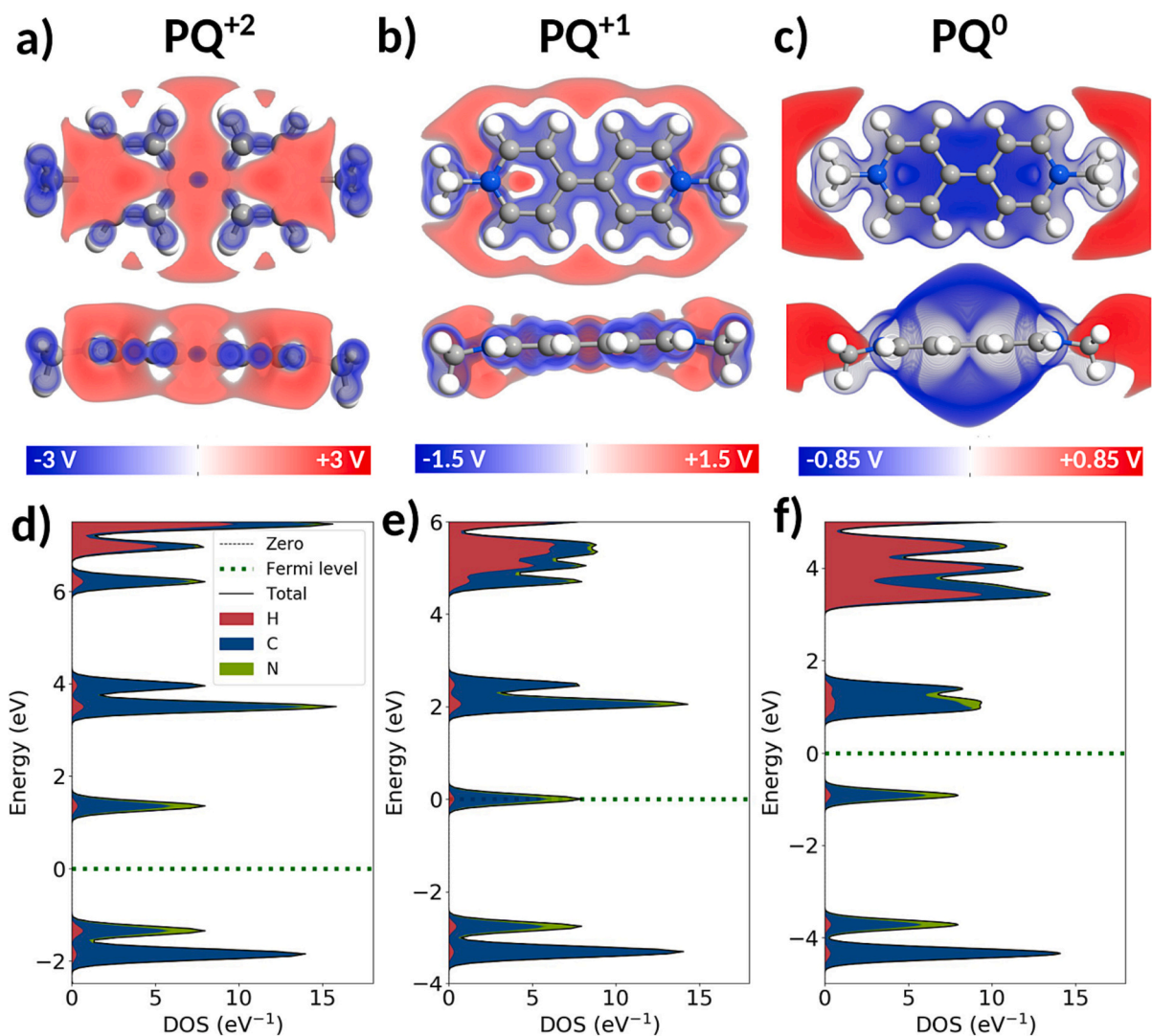
Fig. 6. Molecular electrostatic potential maps of the PQ molecule in two perspectives for (a) oxidized state PQ^{+2}, (b) partially reduced state PQ^{+1}, and (c) fully reduced state PQ^0. Scale bars are given below maps for each molecule. Density of states spectra projected to atomic contribution to the molecular orbitals for (d) PQ^{+2}, (e) PQ^{+1} (corresponding to PQ$_1$), and (f) PQ^0 (corresponding to PQ$_2$), respectively. Green dotted lines indicate the Fermi levels.

Table 5
Comparison of the PQ adsorption energies on three carbon-based electrode models with different placements of the boron atoms.

Adsorption energies [eV]	Pristine	Surface-boron	Bulk-boron
Diamond (220)	0.76	−2.66	−2.67
Graphite (0002)	−1.40	−1.50	−1.45
Graphite (11–20)	−1.70	−2.49	−2.42

Table 6
Free energies of the electron transfer were calculated for the PQ molecule adsorbed on the bulk-boron-doped electrode models.

Electron transfer energies [eV]	First transfer	Second transfer
Pristine molecule	5.00	3.19
Adsorbed on boron-doped diamond (220)	4.74	5.70
Adsorbed on boron-doped graphite (0002)	4.62	5.63
Adsorbed on boron-doped graphite (11–20)	4.81	5.63

transfer to the PQ molecule.

Considering that the PQ molecule in its oxidized state carries mostly positive charges, a surface that is suitable for PQ adsorption and further

electrochemical detection (see Section 3.5) should have a cloud of negative charge extending into the space. Electrostatic potential maps of the three surfaces are given in Fig. 7(a) to (c). In general, the map corresponding to the boron-doped diamond (220) shows a mixed pattern of the negative polarizations of atomic cores and positive polarizations of the areas between atoms (i.e. bonds). This environment is optimal for PQ adsorption, which is in line with the strongly negative adsorption energy calculated in Table 5. The resulting slab geometry after adsorption (Fig. 7(d)) exhibits a 3.1 Ang distance between the first atomic layer of the BDD and the plane of the PQ rings. Moreover, the electron density map shows a weak overlap of the two densities at the level of 0.05 electrons/Ang^3. These two observations indicate the non-covalent binding between the surface and the molecule, which strongly suggests the OSET type of reaction in the electrochemical experiments given in Section 3.5.

On the other hand, the graphite (0002) surface is almost exclusively positively charged and extends several Angstroms in the direction perpendicular to the slab. In such an electrostatic environment, the adsorption is not favorable. This statement is confirmed by the less negative value of the adsorption energy (Table 5) and the features on the electron density map of the system after adsorption (Fig. 7(e)). It is easy to see that the overlap of molecular electron densities across the
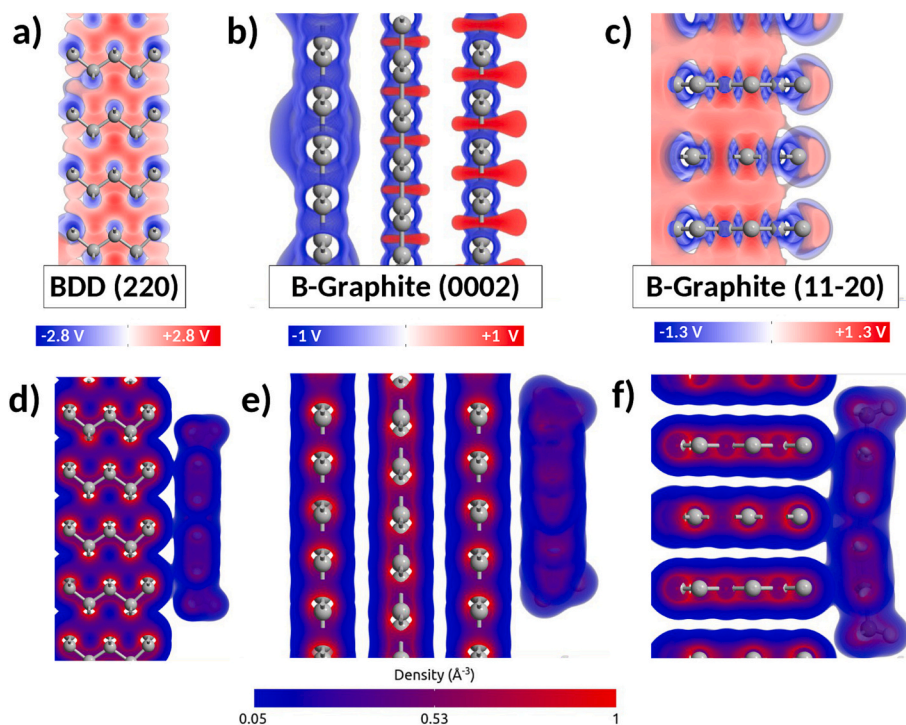
Fig. 7. Molecular electrostatic potential maps of pristine slabs consisting of (a) boron-doped diamond (220), (b) flat boron-doped graphite (0002), and (c) vertical boron-doped graphite (11–20). Scale bars are given below maps for each molecule. Electron density maps of the slabs with adsorbed PQ molecule illustrating surface–adsorbate interactions for (d) boron-doped diamond (220), (e) flat boron-doped graphite (0002), and (f) vertical boron-doped graphite (11–20). The electron density scale bar is given below the slabs and is the same for all three systems.

interface is negligible with a 3.3 Ang distance between atomic planes.

Lastly, the vertical graphite (11–20) exhibits a hybrid pattern of electrostatic charges across the surface with a negatively charged envelope extending to the space. This pattern is analogous to the case of the BDD and should favor adsorption of the PQ molecule, which confirms that both the experimental B:CNW and BDD electrodes show a strong affinity toward PQ detection. Indeed, the strongly negative value of the free energy in Table 5 and the overlap of the electron density in Fig. 7(f) support this prediction. The carbon-carbon distances between the graphite edge and the aryl-aryl linkage are the smallest among all surfaces and are equal to 2.5 Ang. This setup is more optimal for electron transfer than in the case of BDD, which is supported by the corresponding free energy value in Table 6 and experimental results in PQ detection given in Fig. 3. Additionally, the fact that the B:CNW electrode is comprised of both planar (0002) and vertical (11–20) graphite with different adsorption and charge transfer energies might explain the presence of the two different linear ranges reported in Fig. 4. The first 0.1–1.0 μM range should correspond to adsorption of the PQ on the vertical graphite, having a lower energy barrier for the charge transfer and fewer adsorption sites. The latter 2–12 μM range most presumably corresponds to adsorption on the planar graphite, exhibiting a higher barrier for charge transfer, but more adsorption sites and – in consequence – electrochemically active surface area (EASA). Considering that the B:CNW electrode exhibits a fractal structure [55] with a large EASA, both types of adsorption (on planar and vertical graphite) are possible with an overall significantly larger number of sites available for PQ adsorption in comparison to the flat BDD.

Some works report that the molecule in the highest oxidation state is no longer planar [56], and the dihedral angle between the rings is equal to ca. 20°. This might be a rationale for the relatively high second charge transfer energy on the surfaces compared to the pristine slab. Although such a conformational change was not captured by the PBE level of theory, it might have been recognized using e.g. hybrid functionals. Both the BDD and BCNW electrode models exhibit similar energetics of PQ

adsorption. However, the vertically oriented graphite provides the highest electron density overlap and smallest carbon-carbon distance, which is relevant for the electron transfer. Moreover, it is the flat graphite that exhibits the highest catalytic effect in terms of the first electron reduction. Therefore, the presented simulations point to the conclusion that B:CNWs are superior to BDD in terms of PQ electrochemical recognition. The comparative study of B:CNWs and BDD showed that the selection of potential electrodes is crucial for the electrochemical detection of highly toxic pesticides or herbicides. The higher sensitivity, lower LOD, and excellent performance of B:CNWs in the detection of PQ in real water samples suggest its potential for use in environmental monitoring and assessment.

4. Conclusions

A comparison study of BCNW and BDD electrodes was performed for the electrochemical detection of the highly toxic herbicide paraquat (PQ). The surface area of the B:CNW samples was larger than for the BDD samples, as can be seen in the SEM images. The surface morphology of the BDD was microcrystalline whereas the B:CNWs had a 3D structure with vertical graphene planes. More sp^3 hybridized carbon than sp^2 hybridized carbon was present in the B:CNW samples, confirming the presence of graphene. The reverse was observed for the BDD samples. Raman spectroscopy also confirmed similar trends. The B:CNW samples showed higher CV peak currents than the BDD samples. B:CNWs also had a lower peak-to-peak separation for the ferro/ferri redox probe than the BDD. The comparison study was performed for experimental parameter optimization also among BDD and B:CNWs. Notably, only two transitions of PQ were observed, among which PQ_1 was the dominant one. The peak current of PQ_1 was found to be higher than PQ_2 during deposition potential optimization. The B:CNWs displayed a higher current profile than the BDD samples for the detection of PQ using the SWV method. The B:CNWs also revealed an enhanced sensitivity of 11 μA/μM.cm^2 compared to BDD's sensitivity of only 2.23 μA/

$\mu M.cm^2$ in the same concentration range. The real water sample analysis also showed a recovery of less than 5 % for the B:CNW samples. The selectivity of B:CNWs for electrochemical sensing of PQ was investigated with other pesticides as interferent. The concentration of the interferent was 10 times higher than PQ, has shown enhanced performance with variation below 10 %. These results were also confirmed by the DFT calculations showing a higher propensity of the B:CNW electrode models toward PQ electrocatalytic reduction. Hence, it was well established that the B:CNWs showed enhanced electrochemical sensing properties over the BDD samples, with more studies that can be performed using additional surface functionalization. The use of these surfaces provided a more sensitive and efficient method of detecting hazardous contaminants in tap water, which can aid in preventing their harmful effects on human health and the environment.

CRediT authorship contribution statement

Sourav Sain: Conceptualization, Investigation, Validation, Writing – original draft, Visualization, Data curation. **Mateusz Ficek:** Resources, Writing – original draft. **Adrian Olejnik:** Formal analysis, Writing – original draft, Visualization. **Mirosław Sawczak:** Formal analysis, Validation, Writing – original draft, Visualization. **Robert Bogdanowicz:** Conceptualization, Methodology, Investigation, Writing – original draft, Writing – review & editing, Visualization, Supervision, Funding acquisition. **Susanta Sinha Roy:** Conceptualization, Resources, Writing – review & editing, Supervision, Funding acquisition.

Declaration of competing interest

The authors declare no competing financial interest.

Data availability

Data will be made available on request.

Acknowledgments

Appendix A. Supplementary data

Supplementary data to this article can be found online at https://doi. org/10.1016/j.diamond.2023.110504.

References

[1] X.-G. Chu, X.-Z. Hu, H.-Y. Yao, Determination of 266 pesticide residues in apple juice by matrix solid-phase dispersion and gas chromatography–mass selective detection, J. Chromatogr. A 1063 (2005) 201–210.
[2] R. Eisler, Eisler's Encyclopedia of Environmentally Hazardous Priority Chemicals, Elsevier, 2007.
[3] W.-T. Tsai, A review on environmental exposure and health risks of herbicide paraquat, Toxicol. Environ. Chem. 95 (2013) 197–206.
[4] R.H. Bromilow, Paraquat and sustainable agriculture, Pest Manag. Sci. 60 (2004) 340–349.
[5] F. Laghrib, M. Bakasse, S. Lahrich, M. El Mhammedi, Electrochemical sensors for improved detection of paraquat in food samples: a review, Mater. Sci. Eng. C 107 (2020) 110349.
[6] M. El Mhammedi, M. Bakasse, A. Chtaini, Electrochemical studies and square wave voltammetry of paraquat at natural phosphate modified carbon paste electrode, J. Hazard. Mater. 145 (2007) 1–7.
[7] S. El Kasmi, S. Lahrich, A. Farahi, M. Zriouil, M. Ahmamou, M. Bakasse, M. El Mhammedi, Electrochemical determination of paraquat in potato, lemon, orange

[8] M. Ito, Y. Hori, M. Fujisawa, A. Oda, S. Katsuyama, Y. Hirose, T. Yoshioka, Rapid analysis method for paraquat and diquat in the serum using ion-pair high-performance liquid chromatography, Biol. Pharm. Bull. 28 (2005) 725–728.
[9] L. Chen, S. Wang, O. Sha, Y. Wang, X. Yin, X. Chen, Magnetic solid-phase extraction using Fe 3 O 4@ SiO 2 magnetic nanoparticles followed by UV-vis spectrometry for determination of paraquat in plasma and urine samples, J. Anal. Methods Chem. (2017), 8704639, 1–9.
[10] L.R. Guterres Silva, J. Santos Stefano, R. Cornélio Ferreira Nocelli, B. Campos Janegitz, 3D electrochemical device obtained by additive manufacturing for sequential determination of paraquat and carbendazim in food samples, Food Chem. 406 (2023), 135038.
[11] M. Li, X. Wang, Y. Zhu, X. Jia, S. Zhang, H. Wang, Y. Li, G. Hu, Fe2O3-decorated boron/nitrogen-co-doped carbon nanosheets as an electrochemical sensing platform for ultrasensitive determination of paraquat in natural water, Chin. Chem. Lett. 34 (2023), 107299.
[12] H. Zhang, K.-T. Huang, L. Ding, J. Yang, Y.-W. Yang, F. Liang, Electrochemical determination of paraquat using a glassy carbon electrode decorated with pillararene-coated nitrogen-doped carbon dots, Chin. Chem. Lett. 33 (2022) 1537–1540.
[13] I. Tzouvadaki, N. Aliakbarinodehi, D.D. Pineda, G. De Micheli, S. Carrara, Graphene nanowalls for high-performance chemotherapeutic drug sensing and anti-fouling properties, Sensors Actuators B Chem. 262 (2018) 395–403.
[14] K. Prasad, C.D. Bandara, S. Kumar, G.P. Singh, B. Brockhoff, K. Bazaka, K. Ostrikov, Effect of precursor on antifouling efficacy of vertically-oriented graphene nanosheets, Nanomaterials 7 (2017) 170.
[15] J. Svítková, T. Ignat, Ľ. Švorc, J. Labuda, J. Barek, Chemical modification of boron-doped diamond electrodes for applications to biosensors and biosensing, Crit. Rev. Anal. Chem. 46 (2016) 248–256.
[16] M. Wei, G. Zeng, Q. Lu, Determination of organophosphate pesticides using an acetylcholinesterase-based biosensor based on a boron-doped diamond electrode modified with gold nanoparticles and carbon spheres, Microchim. Acta 181 (2014) 121–127.
[17] M. Medina-Sánchez, C.C. Mayorga-Martinez, T. Watanabe, T.A. Ivandini, Y. Honda, F. Pino, K. Nakata, A. Fujishima, Y. Einaga, A. Merkoçi, Microfluidic platform for environmental contaminants sensing and degradation based on boron-doped diamond electrodes, Biosens. Bioelectron. 75 (2016) 365–374.
[18] P. Niedziałkowski, Z. Cebula, N. Malinowska, W. Białobrzeska, M. Sobaszek, M. Ficek, R. Bogdanowicz, J.S. Anand, T. Ossowski, Comparison of the paracetamol electrochemical determination using boron-doped diamond electrode and boron-doped carbon nanowalls, Biosens. Bioelectron. 126 (2019) 308–314.
[19] K. Siuzdak, M. Ficek, M. Sobaszek, J. Ryl, M. Gnyba, P. Niedziałkowski, N. Malinowska, J. Karczewski, R. Bogdanowicz, Boron-enhanced growth of micron-scale carbon-based nanowalls: a route toward high rates of electrochemical biosensing, ACS Appl. Mater. Interfaces 9 (2017) 12982–12992.
[20] W. Białobrzeska, M. Ficek, B. Dec, S. Osella, B. Trzaskowski, A. Jaramillo-Botero, M. Pierpaoli, M. Rycewicz, Y. Dashkevich, T. Łęga, N. Malinowska, Z. Cebula, D. Bigus, D. Firganek, E. Bięga, K. Dziąbowska, M. Brodowski, M. Kowalski, M. Panasiuk, B. Gromadzka, S. Żołędowska, D. Nidzworski, K. Pyrć, W.A. Goddard, R. Bogdanowicz, Performance of electrochemical immunoassays for clinical diagnostics of SARS-CoV-2 based on selective nucleocapsid N protein detection: boron-doped diamond, gold and glassy carbon evaluation, Biosens. Bioelectron. 209 (2022), 114222.
[21] R. Bogdanowicz, M. Ficek, M. Sobaszek, A. Nosek, Ł. Gołuński, J. Karczewski, A. Jaramillo-Botero, W.A. Goddard III, M. Bockrath, T. Ossowski, Growth and isolation of large area boron-doped nanocrystalline diamond sheets: a route toward diamond-on-graphene heterojunction, Adv. Funct. Mater. 29 (2019) 1805242.
[22] A. Olejnik, M. Ficek, M. Szkodo, A. Stanisławska, J. Karczewski, J. Ryl, A. Dołęga, K. Siuzdak, R. Bogdanowicz, Tailoring diffusional fields in zwitterion/dopamine copolymer electropolymerized at carbon nanowalls for sensitive recognition of neurotransmitters, ACS Nano 16 (2022) 13183–13198.
[23] M. Ficek, B. Dec, K.J. Sankaran, K. Gajewski, P. Tatarczak, I. Wlasny, A. Wysmolek, K. Haenen, T. Gotszalk, R. Bogdanowicz, Stable field electron emission and plasma illumination from boron and nitrogen co-doped edge-rich diamond-enhanced carbon nanowalls, Adv. Mater. Interfaces 8 (2021) 2100464.
[24] H. Liu, M. Chen, Y. Lin, Y. Liu, Electrochemical study of the herbicide paraquat based on a graphene-zinc oxide nanocomposite, Int. J. Electrochem. Sci. 12 (2017) 8599–8608.
[25] M.S. José, A. Emilio, D.G. Julian, G. Alberto, J. Javier, O. Pablo, S.-P. Daniel, The SIESTA method for ab initio order-N materials simulation, J. Phys. Condens. Matter 14 (2002) 2745.
[26] N. Troullier, J.L. Martins, Efficient pseudopotentials for plane-wave calculations, Phys. Rev. B 43 (1991) 1993–2006.
[27] P. Niedzialkowski, A. Koterwa, A. Olejnik, A. Zielinski, K. Gornicka, M. Brodowski, R. Bogdanowicz, J. Ryl, Deciphering the molecular mechanism of substrate-induced assembly of gold nanocube arrays toward an accelerated electrocatalytic effect employing heterogeneous diffusion field confinement, Langmuir 38 (2022) 9597–9610.
[28] D. Medeiros de Araújo, P. Cañizares, C.A. Martínez-Huitle, M.A. Rodrigo, Electrochemical conversion/combustion of a model organic pollutant on BDD anode: role of sp3/sp2 ratio, Electrochem. Commun. 47 (2014) 37–40.
[29] M. Pierpaoli, P. Jakobczyk, M. Sawczak, A. Łuczkiewicz, S. Fudala-Książek, R. Bogdanowicz, Carbon nanoarchitectures as high-performance electrodes for the electrochemical oxidation of landfill leachate, J. Hazard. Mater. 401 (2021), 123407.

[30] M. Sobaszek, K. Siuzdak, J. Ryl, M. Sawczak, S. Gupta, S.B. Carrizosa, M. Ficek, B. Dec, K. Darowicki, R. Bogdanowicz, Diamond phase (sp3-C) rich boron-doped carbon nanowalls (sp2-C): physicochemical and electrochemical properties, J. Phys. Chem. C 121 (2017) 20821–20833.

[31] S.K. Sethy, M. Ficek, K.J. Sankaran, S. Sain, A.R. Tripathy, S. Gupta, J. Ryl, S. Sinha Roy, N.-H. Tai, R. Bogdanowicz, Nitrogen-incorporated boron-doped nanocrystalline diamond nanowires for microplasma illumination, ACS Appl. Mater. Interfaces 13 (2021) 55687–55699.

[32] S. Garcia-Segura, E.V. Dos Santos, C.A. Martínez-Huitle, Role of sp3/sp2 ratio on the electrocatalytic properties of boron-doped diamond electrodes: a mini review, Electrochem. Commun. 59 (2015) 52–55.

[33] E. Bourgeois, E. Bustarret, P. Achatz, F. Omnès, X. Blase, Impurity dimers in superconducting B-doped diamond: experiment and first-principles calculations, Phys. Rev. B 74 (2006), 094509.

[34] M. Bernard, C. Baron, A. Deneuville, About the origin of the low wave number structures of the Raman spectra of heavily boron doped diamond films, Diam. Relat. Mater. 13 (2004) 896–899.

[35] P. Szirmai, T. Pichler, O.A. Williams, S. Mandal, C. Bäuerle, F. Simon, A detailed analysis of the Raman spectra in superconducting boron doped nanocrystalline diamond, Phys. Status Solidi B 249 (2012) 2656–2659.

[36] A.C. Ferrari, J. Robertson, Resonant Raman spectroscopy of disordered, amorphous, and diamondlike carbon, Phys. Rev. B 64 (2001), 075414.

[37] Y.A. Kim, K. Fujisawa, H. Muramatsu, T. Hayashi, M. Endo, T. Fujimori, K. Kaneko, M. Terrones, J. Behrends, A. Eckmann, C. Casiraghi, K.S. Novoselov, R. Saito, M. S. Dresselhaus, Raman spectroscopy of boron-doped single-layer graphene, ACS Nano 6 (2012) 6293–6300.

[38] Y. Hishiyama, H. Irumano, Y. Kaburagi, Y. Soneda, Structure, Raman scattering, and transport properties of boron-doped graphite, Phys. Rev. B 63 (2001), 245406.

[39] A. Ambrosi, C.K. Chua, A. Bonanni, M. Pumera, Electrochemistry of graphene and related materials, Chem. Rev. 114 (2014) 7150–7188.

[40] A.J. Bard, L.R. Faulkner, H.S. White, Electrochemical Methods: Fundamentals and Applications, John Wiley & Sons, 2022.

[41] A. Dettlaff, M. Rycewicz, M. Ficek, A. Wieloszyńska, M. Szala, J. Ryl, R. Bogdanowicz, Conductive printable electrodes tuned by boron-doped nanodiamond foil additives for nitroexplosive detection, Microchim. Acta 189 (2022) 270.

[42] T. Paramalinggam, A.R.M. Yusoff, M.S. Qureshi, Z.A. Shah, P. Sathishkumar, Z. Yusop, M. Khalid, F.M. Khokhar, Determination of paraquat dichloride from water samples using differential pulse cathodic stripping voltammetry, Russ. J. Electrochem. 54 (2018) 1155–1163.

[43] P.K. Roy, A. Ganguly, W.-H. Yang, C.-T. Wu, J.-S. Hwang, Y. Tai, K.-H. Chen, L.-C. Chen, S. Chattopadhyay, Edge promoted ultrasensitive electrochemical detection of organic bio-molecules on epitaxial graphene nanowalls, Biosens. Bioelectron. 70 (2015) 137–144.

[44] W. Zheng, X. Zhao, W. Fu, Review of vertical graphene and its applications, ACS Appl. Mater. Interfaces 13 (2021) 9561–9579.

[45] Y. Yu, Y. Zhou, L. Wu, J. Zhi, Electrochemical biosensor based on boron-doped diamond electrodes with modified surfaces, Int. J. Electrochem. 2012 (2012).

[46] R.M. de Almeida, M. Yonamine, Gas chromatographic–mass spectrometric method for the determination of the herbicides paraquat and diquat in plasma and urine samples, J. Chromatogr. B 853 (2007) 260–264.

[47] A. Chen, B. Shah, Electrochemical sensing and biosensing based on square wave voltammetry, Anal. Methods 5 (2013) 2158–2173.

[48] Z. Zhao, F. Zhang, Z. Zhang, A facile fluorescent "turn-off" method for sensing paraquat based on pyranine-paraquat interaction, Spectrochim. Acta A Mol. Biomol. Spectrosc. 199 (2018) 96–101.

[49] M.A. Dominguez, M. Insausti, R. Ilari, G.P. Zanini, Fluorescence enhancement novel green analytical method for paraquat herbicide quantification based on immobilization on clay, Analyst 144 (2019) 3357–3363.

[50] S. Sain, S. Roy, A. Mathur, V.M. Rajesh, D. Banerjee, B. Sarkar, S.S. Roy, Electrochemical sensors based on flexible laser-induced graphene for the detection of paraquat in water, ACS Appl Nano Mater. 5 (2022) 17516–17525.

[51] H. Hou, B. Wang, Solvent-dependent mechanistic aspects for the redox reaction of paraquat in basic solution, Int. J. Quantum Chem. 121 (2021), e26757.

[52] R. Botta, P. Eiamchai, M. Horprathum, S. Limwichean, C. Chananonnawathorn, V. Patthanasettakul, R. Maezono, A. Jomphoak, N. Nuntawong, 3D structured laser engraves decorated with gold nanoparticle SERS chips for paraquat herbicide detection in environments, Sensors Actuators B Chem. 304 (2020), 127327.

[53] D.A. Kleier, G.H. Weeks, Electronic structure and conformational analysis of paraquat in three oxidation states, J. Mol. Struct. (THEOCHEM) 148 (1986) 25–31.

[54] S. Kreisig, A. Tarazona, E. Koglin, The adsorption aspects of paraquat on silver electrode surfaces: a SERS microprobe study, Electrochim. Acta 42 (1997) 3335–3344.

[55] M. Pierpaoli, M. Ficek, P. Jakóbczyk, J. Karczewski, R. Bogdanowicz, Self-assembly of vertically orientated graphene nanostructures: multivariate characterisation by Minkowski functionals and fractal geometry, Acta Mater. 214 (2021), 116989.

[56] M. Pateiro-Moure, M. Arias-Estévez, J. Simal-Gándara, Competitive and non-competitive adsorption/desorption of paraquat, diquat and difenzoquat in vineyard-devoted soils, J. Hazard. Mater. 178 (2010) 194–201.